

Statistical image-domain multimaterial decomposition for dual-energy CT

Yi Xue

Sir Run Run Shaw Hospital, Zhejiang University School of Medicine, Institute of Translational Medicine, Zhejiang University, Hangzhou, Zhejiang 310009, China
Key Laboratory of Biomedical Engineering of Ministry of Education, Zhejiang University, Hangzhou, Zhejiang 310009, China

Ruoshui Ruan

University of Michigan–Shanghai Jiao Tong University Joint Institute, Shanghai Jiao Tong University, Shanghai 200240, China

Xiuhua Hu

Sir Run Run Shaw Hospital, Zhejiang University School of Medicine, Institute of Translational Medicine, Zhejiang University, Hangzhou, Zhejiang 310009, China

Yu Kuang

Department of Medical Physics, University of Nevada, 4505 S Maryland Pkwy, Box 453037, Las Vegas, NV 89154-3037, USA

Jing Wang

Sir Run Run Shaw Hospital, Zhejiang University School of Medicine, Institute of Translational Medicine, Zhejiang University, Hangzhou, Zhejiang 310009, China

Yong Long^{a)}

University of Michigan–Shanghai Jiao Tong University Joint Institute, Shanghai Jiao Tong University, Shanghai 200240, China

Tianye Niu^{a)}

Sir Run Run Shaw Hospital, Zhejiang University School of Medicine, Institute of Translational Medicine, Zhejiang University, Hangzhou, Zhejiang 310009, China

Key Laboratory of Biomedical Engineering of Ministry of Education, Zhejiang University, Hangzhou, Zhejiang 310009, China

(Received 2 October 2016; revised 12 December 2016; accepted for publication 27 December 2016; published 21 February 2017)

Purpose: Dual-energy CT (DECT) enhances tissue characterization because of its basis material decomposition capability. In addition to conventional two-material decomposition from DECT measurements, multimaterial decomposition (MMD) is required in many clinical applications. To solve the ill-posed problem of reconstructing multi-material images from dual-energy measurements, additional constraints are incorporated into the formulation, including volume and mass conservation and the assumptions that there are at most three materials in each pixel and various material types among pixels. The recently proposed flexible image-domain MMD method decomposes pixels sequentially into multiple basis materials using a direct inversion scheme which leads to magnified noise in the material images. In this paper, we propose a statistical image-domain MMD method for DECT to suppress the noise.

Methods: The proposed method applies penalized weighted least-square (PWLS) reconstruction with a negative log-likelihood term and edge-preserving regularization for each material. The statistical weight is determined by a data-based method accounting for the noise variance of high- and low-energy CT images. We apply the optimization transfer principles to design a serial of pixel-wise separable quadratic surrogates (PWSQS) functions which monotonically decrease the cost function. The separability in each pixel enables the simultaneous update of all pixels.

Results: The proposed method is evaluated on a digital phantom, Catphan©600 phantom and three patients (pelvis, head, and thigh). We also implement the direct inversion and low-pass filtration methods for a comparison purpose. Compared with the direct inversion method, the proposed method reduces noise standard deviation (STD) in soft tissue by 95.35% in the digital phantom study, by 88.01% in the Catphan©600 phantom study, by 92.45% in the pelvis patient study, by 60.21% in the head patient study, and by 81.22% in the thigh patient study, respectively. The overall volume fraction accuracy is improved by around 6.85%. Compared with the low-pass filtration method, the root-mean-square percentage error (RMSE(%)) of electron densities in the Catphan©600 phantom is decreased by 20.89%. As modulation transfer function (MTF) magnitude decreased to 50%, the proposed method increases the spatial resolution by an overall factor of 1.64 on the digital phantom, and 2.16 on the Catphan©600 phantom. The overall volume fraction accuracy is increased by 6.15%.

Conclusions: We proposed a statistical image-domain MMD method using DECT measurements. The method successfully suppresses the magnified noise while faithfully retaining the quantification accuracy and anatomical structure in the decomposed material images. The proposed method is practical and promising for advanced clinical applications using DECT imaging. © 2017 American

Association of Physicists in Medicine [https://doi.org/10.1002/mp.12096]

Key words: dual-energy CT (DECT), image-domain, multi-material decomposition (MMD), noise suppression, optimization transfer, penalized weighted least-square (PWLS)

1. INTRODUCTION

Spectral CT enhances tissue characterization because of its basis materials' decomposition capability.^{1–9} In essence, two basis materials with various linear attenuation coefficients (e.g., bone and soft tissue) can be reconstructed using dual-energy CT (DECT) technique accurately.^{4–9} In clinical applications, three or more component images are usually required.^{1–3,10,11} For example, liver-fat quantification requires a four-material composition: liver tissue, blood, fat, and contrast agent.^{1–3} One method to achieve this is using expensive hardware, for example, energy-sensitive photon-counting detectors, to acquire multienergy projection data. This paper proposes a multimaterial decomposition (MMD) method using conventional dual-energy measurements which are available from clinical DECT scanners. For example, dual-energy measurements can be acquired from fast kVp-switching,^{12,13} dual-source^{13–15}, or dual-layer detectors^{13,16} DECT scanners.

Dual-energy CT methods can be classified into three categories: projection-domain, image-domain, and direct reconstruction methods.¹⁷ Projection-domain methods decompose DECT measurements into sinograms of basis materials and generate material images using conventional reconstruction algorithms. These methods avoid beam-hardening artifacts because the material-specific projections are estimated prior to image reconstruction.^{5,18} One major challenge for this type of methods is the calibration of spectral transmission model which is nonlinear and computationally expensive. Image-domain methods apply standard reconstruction techniques to obtain low- and high-energy CT images, and decompose them into basis material images using linear approximation of decomposition process.^{1–4,19,20} Mendonça et al. proposed an image-domain pixel-wise MMD method for DECT.^{1,2} This method assumes three basis materials at the most within each pixel and the material types alter among the pixels. The mass and volume conservation are also included as the constraints. It suffers from magnified noise in the decomposed basis images since direct inversion at each pixel is used to estimate volume fractions of basis materials. Long and Fessler proposed a direct MMD method for DECT using penalized-likelihood (PL) reconstruction with edge-preserving regularization for each material.³ This method has the advantages of modeling the physics of spectral transmission exactly, incorporating similar constraints as the method proposed by Mendonça et al.^{1,2} to its CT object model, and significantly decreasing noise and cross-artifacts in the decomposed material images. Nevertheless, it is computationally expensive due to the repeated forward projection of material images and backward projection of the measurements at low and high energies and the modeling of

polyenergetic spectra. We also proposed an image-domain method,⁴ which is an iterative dual-material decomposition with noise suppression using least-square estimation and edge-preserving regularization. In clinical applications, the detected objects have more compositions and the two-material decomposition sometimes is inadequate to fully meet the clinical needs.

The decomposition procedure of DECT measurements is highly sensitive to noise fluctuation due to the overlap of x-ray spectra at low and high energies. To tackle the obstacle, we propose an improved decomposition method to achieve the multimaterial decomposition (MMD) in this paper. Assuming similar constraints applied in previous MMD methods for DECT,^{1–3} we investigate noise suppression in image-domain MMD method. The cost function of the proposed method is in the form of penalized weighted least-square (PWLS) estimation with edge-preserving regularization. The statistical weight is determined by a data-based method accounting for the noise variance of high- and low-energy CT images. The optimization transfer principle is applied to design a pixel-wise separable quadratic surrogate (PWSQS) function in each iteration to reduce the cost function monotonically.³ The separability in each pixel enables simultaneous update of all pixels. The proposed method is evaluated on one digital phantom, one physical phantom (i.e., Catphan©600 evaluation phantom) and three sets of patient data. Compared with the image-domain direct inversion method, the proposed method can significantly suppress noise while faithfully retaining the anatomical structure and decomposition accuracy.

2. METHODS

2.A. Object model for multimaterial decomposition

Multimaterial decomposition (MMD) from DECT measurements is an ill-posed problem since multiple sets of images are estimated from two sets of measurements associated with low and high energies. To solve this ill-posed problem, we apply constraints of volume and mass conservation,^{1–3,11} and assume that each pixel contains at most three materials and the material composition, that is, material-triplet, varies among pixels.^{1–3}

With mass and volume conservation, the spatially and energy-dependent attenuation distribution $\vec{\mu}_E$ is

$$\vec{\mu}_E = \sum_{l=1}^{L_0} \mu_{lE} \vec{x}_l, \quad (1)$$

where \vec{x}_l denotes the volume fraction image of the l -th material and is unitless. L_0 is the total number of basis material types, and μ_{lE} is the linear attenuation coefficient (LAC) of

the l -th material at energy level E . According to the constraints of volume conservation, volume fraction \vec{x}_l satisfies the sum-to-one and box constraints, that is,

$$\sum_{l=1}^{L_0} x_{lp} = 1, \forall p, \quad (2)$$

$$a_l \leq x_{lp} \leq b_l, \forall l, p, \quad (3)$$

where p indicates the p -th pixel. We relax the lower bound a_l of the box constraint to be slightly smaller than 0, and the upper bound b_l to be slightly greater than 1.^{3,21} Under the assumptions that each pixel contains at most three basis materials and triplet-material composition change among pixels,³ volume fraction \vec{x}_l also satisfies the following constraint,

$$\sum_{l=1}^{L_0} I_{\{x_{lp} \neq 0\}} \leq 3, \forall p, \quad (4)$$

where $I_{\{\cdot\}}$ denotes the indicator function, which is 1 if the condition is satisfied and 0 otherwise.

We define Ω as a material triplet library containing all the possible triplets from preselected materials of interest.¹⁻³ The image-domain direct inversion method proposed by Mendonça et al.^{1,2} solves the linear system in Eqs. (1) and (2) for a given pixel in the triplet library Ω . If only one solution satisfies the box constraint $0 \leq x_l \leq 1, \forall l$, the optimal solution is found. If more than one feasible solution exists, the solution with the minimal Euclidean distance to the LAC pair is selected as the optimal solution from all the triplets in the feasible solution pool. If no feasible solution is found, the box constraint is relaxed to find the possible triplets, and the triplet with minimal Hausdorff distance to the LAC pair is selected as the optimal solution.¹ This method yields noisy material images due to the unregularized inversion.³

2.B. Statistical image-domain multimaterial decomposition

To suppress noise in the decomposed material images, we employ a penalized weighted least-square (PWLS) method to estimate multi-material images from high- and low-energy CT images. We model the high- and low-energy CT images as independent Gaussian random variables, that is,

$$\mu_{Ep} \sim N((\vec{a}_E)^T \vec{x}_p, \text{var}(\mu_{Ep})), \quad (5)$$

where the measurement μ_{Ep} corresponding to the p -th pixel value at energy level E , T denotes the transpose operator, $\vec{a}_E = [\mu_{1E}, \dots, \mu_{L_0E}]^T$, $\vec{x}_p = [x_{1p}, \dots, x_{L_0p}]^T$ is a vector of L_0 elements at the p -th pixel, and $\text{var}(\mu_{Ep})$ is the variance. The probability density function (pdf) is

$$p(\mu_{Ep}; \vec{x}_p) = \frac{1}{\sqrt{2\pi \text{var}(\mu_{Ep})}} \exp\left(-\frac{(\mu_{Ep} - (\vec{a}_E)^T \vec{x}_p)^2}{2\text{var}(\mu_{Ep})}\right). \quad (6)$$

The corresponding negative log-likelihood for independent measurements μ_{Ep} has the form,

$$L(\vec{x}) = -\sum_{E=1}^2 \sum_{p=1}^{N_p} \log(p(\mu_{Ep}; \vec{x}_p)), \quad (7)$$

$$\equiv (A\vec{x} - \vec{\mu})^T V^{-1} (A\vec{x} - \vec{\mu}),$$

where the symbol \equiv indicates “equal to within irrelevant constants independent of \vec{x} ”. N_p is the total number of pixels in one CT image. The $2N_p \times L_0N_p$ system matrix A is defined as

$$A = A_0 \otimes I_{N_p}, \quad (8)$$

where “ \otimes ” denotes the Kronecker product, the $2 \times L_0$ material decomposition matrix A_0 is

$$A_0 = \begin{pmatrix} \mu_{1H} \cdots \mu_{L_0H} \\ \mu_{1L} \cdots \mu_{L_0L} \end{pmatrix}, \quad (9)$$

Here, I_{N_p} denotes the $N_p \times N_p$ identity matrix. $\vec{\mu} = [\vec{\mu}_H^T \vec{\mu}_L^T]^T$ is a $2N_p$ vector where $\vec{\mu}_H$ and $\vec{\mu}_L$ are the high- and low-energy CT images, respectively. $\vec{x} = [\vec{x}_1^T, \dots, \vec{x}_{L_0}^T]^T$ is a L_0N_p vector composed of $\vec{x}_1, \dots, \vec{x}_{L_0}$ basis material images. The statistical weight V is a $2N_p \times 2N_p$ diagonal matrix whose diagonal elements are the noise variance of pixels in the high- and low-energy CT images, that is,

$$V = \text{diag}(\text{var}(\mu_{H1}), \dots, \text{var}(\mu_{HN_p}), \text{var}(\mu_{L1}), \dots, \text{var}(\mu_{LN_p})), \quad (10)$$

where $\text{var}(\mu_{Hp})$ and $\text{var}(\mu_{Lp})$ are the statistical noise variance of the p -th pixel in the high- and low-energy CT images, respectively. The pixel-wise noise variance can be estimated on a serial of CT images acquired from repeated scans on the same object. This method is not practical to implement on clinical patients due to accumulated high radiation dose. In this work, we approximate the noise variance of each pixel in a region composed of homogeneous material of the high/low CT image and calculate the numerical variance as in our previous work.⁴

We estimate volume fraction images \vec{x} of basis materials from noisy high- and low-energy CT images by minimizing the PWLS cost function subject to pixel-wise constraints given in Eqs. (2), (3), and (4) as following,

$$\hat{\vec{x}} = \vec{x} \underset{\text{subject to (2), (3)\&(4)}}{\text{arg min}} \Psi(\vec{x}), \quad (11)$$

$$\Psi(\vec{x}) \triangleq L(\vec{x}) + R(\vec{x}). \quad (12)$$

The material-wise edge-preserving regularization $R(\vec{x})$ is as following,³

$$R(\vec{x}) = \sum_{l=1}^{L_0} \beta_l R_l(\vec{x}_l), \quad (13)$$

where the regularizer for the l -th material is³

$$R_l(\vec{x}_l) = \sum_{p=1}^{N_p} \sum_{k \in N_p} \psi_l(x_{lp} - x_{lk}). \quad (14)$$

Here, the potential function ψ_l is a hyperbola³

$$\psi_l(t) = \frac{\delta_l^2}{3} \left(\sqrt{1 + 3 \left(\frac{t}{\delta_l} \right)^2} - 1 \right), \quad (15)$$

and N_{lp} is a neighborhood of pixel x_{lp} . The regularization parameters β_l and δ_l are chosen for different materials separately to achieve the desired edge preservation and noise-resolution tradeoff for each material image.

2.C. Optimization Algorithm

Minimizing the cost function $\Psi(\vec{x})$ in Eq. (12) directly is difficult because of the nonconvex constraints on each pixel. We thus apply the optimization transfer principles^{22–25} to find a series of pixel-wise separable quadratic surrogate (PWSQS) functions $\phi^{(n)}(\vec{x})$ at each iteration to decrease the cost function monotonically.³ The separability in pixels enables parallelization of the PWSQS algorithm. The PWSQS function $\phi^{(n)}(\vec{x})$ at the n -th iteration is:

$$\phi^{(n)}(\vec{x}) \equiv \sum_{p=1}^{N_p} \phi_p^{(n)}(\vec{x}_p), \quad (16)$$

where $\phi_p^{(n)}(\vec{x}_p)$ denotes the PWSQS function of the p -th pixel. We rewrite the data fidelity term $L(\vec{x})$ in Eq. (7) to show that it is a pixel-wise separable quadratic function as follows,

$$L(\vec{x}) = \sum_{p=1}^{N_p} L_p(\vec{x}_p), \quad (17)$$

where

$$L_p(\vec{x}_p) = (A_0 \vec{x}_p - \vec{\mu}_p)^T V_p^{-1} (A_0 \vec{x}_p - \vec{\mu}_p). \quad (18)$$

Here, $V_p = \text{diag}(\text{var}(\mu_{Hp}), \text{var}(\mu_{Lp}))$ and $\vec{\mu}_p = [\mu_{Hp} \ \mu_{Lp}]^T$.

Similar to our previous work,³ we derive a PWSQS function for the penalty term by applying De Pierro's additive convexity trick^{22,26,27} and use Huber's optimal curvature²⁸ for the potential function $\psi_l(t)$. The PWSQS function for the penalty term in Eq. (13) is:

$$R^{(n)}(\vec{x}) = \sum_{p=1}^{N_p} R_p^{(n)}(\vec{x}_p), \quad (19)$$

where

$$R_p^{(n)}(\vec{x}_p) = R(\vec{x}_p^{(n)}) + \left(\dot{R}_p^{(n)} \right)^T (\vec{x}_p - \vec{x}_p^{(n)}) + \frac{1}{2} (\vec{x}_p - \vec{x}_p^{(n)})^T H_{Rp}^{(n)} (\vec{x}_p - \vec{x}_p^{(n)}). \quad (20)$$

Here, $\dot{R}_p^{(n)}$ and $H_{Rp}^{(n)}$ are the gradient and Hessian of the penalty term about \vec{x}_p , respectively, and

$$\dot{R}_p^{(n)} = \left[\beta_1 \frac{\partial}{\partial x_{1p}} R_1(\vec{x}_1^{(n)}), \dots, \beta_{L_0} \frac{\partial}{\partial x_{L_0 p}} R_{L_0}(\vec{x}_{L_0}^{(n)}) \right]^T, \quad (21)$$

where

$$\frac{\partial}{\partial x_{lp}} R_l(\vec{x}_l^{(n)}) = \sum_{k \in N_{lp}} \psi_l(x_{lp}^{(n)} - x_{lk}^{(n)}), l = 1, \dots, L_0, \quad (22)$$

$$H_{Rp}^{(n)} \triangleq \text{diag} \left\{ 4\beta_l \sum_{k \in N_{lp}} \omega_{\psi_l}(x_{lp}^{(n)} - x_{lk}^{(n)}) \right\}, \text{ where } \omega_{\psi_l}(t) \triangleq \psi_l(t)/t. \quad (23)$$

Combining the PWSQS functions for the data fidelity term and regularization term, we have the PWSQS function for the cost function at the n -th iteration as follows:

$$\begin{aligned} \phi_p^{(n)}(\vec{x}_p) &= L_p(\vec{x}_p) + R_p^{(n)}(\vec{x}_p) \\ &\equiv \frac{1}{2} \vec{x}_p^T H \vec{x}_p + \vec{q}^T \vec{x}_p, \end{aligned} \quad (24)$$

where the Hessian and gradient are

$$H = 2A_0^T V_p^{-1} A_0 + H_{Rp}^{(n)}, \quad (25)$$

$$\vec{q} = 2A_0^T V_p^{-1} A_0 \vec{x}_p^{(n)} - 2A_0^T V_p^{-1} \vec{\mu}_p + \dot{R}_p^{(n)} - H^T \vec{x}_p^{(n)}. \quad (26)$$

To enforce the constraint in Eq. (4), we loop over all the possible triplets in the triplet library Ω and determine the optimal one for each pixel as the triplet minimizing the surrogate of that pixel.³ For each triplet $\tau = (i, j, k) \in \Omega$, the surrogate degenerates to a quadratic function of a vector with three unknowns, $\vec{x}_p(\tau) \triangleq [x_{ip}, x_{jp}, x_{kp}]^T$. Optimizing the degenerated quadratic surrogate under constraints in Eqs. (2) and (3) is a classical convex quadratic programming problem,³ that is,

$$\begin{aligned} \hat{\vec{x}}_p(\tau) &= \vec{x}_p(\tau) \underset{\text{subject to (2) \& (3)}}{\text{arg min}} \phi_p^{(n)}(\vec{x}_p(\tau)), \\ \phi_p^{(n)}(\vec{x}_p(\tau)) &\equiv \frac{1}{2} \vec{x}_p^T(\tau) H(\tau) \vec{x}_p(\tau) + \vec{q}^T(\tau) \vec{x}_p(\tau), \\ \text{s.t. } &\begin{cases} \sum_{l=1}^{L_0} x_{lp} = 1, \\ a_l \leq x_{lp} \leq b_l, \end{cases} \end{aligned} \quad (27)$$

where $H(\tau)$ and $\vec{q}(\tau)$ are formed from elements in H and \vec{q} with indexes corresponding to $\tau = (i, j, k)$, respectively. We solve the convex quadratic programming problem in Eq. (27) using Generalized Sequential Minimization Algorithm (GSMO).²⁹ Table I summarizes the pseudocode of the overall PWSQS algorithm.

The stopping criterion is set as the difference between two adjacent iterations. The program stops when the difference between two adjacent iterations is less than a preset threshold.

2.D. Data acquisition

The proposed method is evaluated using digital phantom, Catphan©600 phantom data, and three sets of patient data. The linear attenuation coefficients in the digital phantom are obtained from the National Institute of Standards and Technology (NIST) database.³⁰ We generate DECT measurements

TABLE I. Pseudocode of the pixel-wise separable quadratic surrogate (PWSQS) algorithm.

1. Initialize $\hat{x}^{(0)}$ using the results of the direct inversion method.^{1,2}
2. **For each iteration** $n = 1, \dots, \text{Niter}$
 - a. Compute Hessian H using Eq. (25).
 - b. Compute gradient \vec{q} using Eq. (26).
 - c. **For each triple** $\tau = (i, j, k) \in \Omega$
 - i. $\vec{x}_p(\tau) \triangleq [x_{ip}, x_{jp}, x_{kp}]^T$, $\vec{x}_p^{(n)}(\tau) \triangleq [x_{ip}^{(n)}, x_{jp}^{(n)}, x_{kp}^{(n)}]^T$, form $H(\tau)$ and $\vec{q}(\tau)$ from elements in H and \vec{q} with indexes corresponding to $\tau = (i, j, k)$, respectively.
 - ii. Find and save the optimal $\hat{x}_p^{(n)}(\tau)$ and the corresponding function value $\phi_p^{(n)}(\hat{x}_p^{(n)}(\tau))$ of the convex quadratic programming problem in Eq. (27) using GSO.

End
 - d. Determine the optimal triplet by comparing all $\phi_p^{(n)}(\hat{x}_p^{(n)}(\tau))$, i.e.,

$$\hat{\tau} = \underset{\tau \in \Omega}{\arg \min} \phi_p^{(n)}(\hat{x}_p^{(n)}(\tau)).$$
 - e. Obtain $\hat{x}_p \equiv \hat{x}_p(\hat{\tau})$ with padded zeros for $l \notin \tau$.
 - f. Update all pixels. $\vec{x}^{(n+1)} = (\vec{x}_1, \dots, \vec{x}_p, \dots, \vec{x}_{N_p})$.

End

at 75 kVp and 140 kVp spectra with 12 mm Al filter, respectively. The high- and low-energy spectra of incident x-ray photons are simulated using Siemens simulator.³¹ The source to detector distance is 1500 mm, and the source to rotation center distance is 1000 mm. The detector is composed of 1024×768 pixels with the physical size of 0.388×0.388 mm² per pixel. A total number of 676 projections over $[0^\circ 360^\circ)$ are acquired. Poisson noise is added to the simulated projection data. The high- and low-energy CT images are reconstructed using the standard filtered back projection (FBP) algorithm^{32,33} with a dimension of 512×512 and a physical size of 0.5×0.5 mm² per pixel.

The Catphan©600 phantom data are acquired on a tabletop cone-beam CT (CBCT) system, whose geometry matches that of a Varian On-Board Imager (OBI) on the Trilogy radiation therapy machine. The CB4030 flat-panel detector (Varian Medical Systems) has 1024×768 pixels with a physical size of 0.388 mm \times 0.388 mm per pixel. The scanned x-ray energies are 75 kVp and 125 kVp with a tube current of 80 mA and a pulse width of 13 ms. In each scan, a total number of 655 projections are acquired over $[0^\circ 360^\circ)$. The projections with scatter contamination inherently suppressed are acquired using a fan-beam geometry with a longitudinal beam width of 15 mm on the detector.³⁴ The reconstructed images have a dimension of 512×512 with a size of 0.5 mm \times 0.5 mm per pixel.

The patient data are scanned by Siemens SOMATOM Definition flash CT scanner and Siemens SOMATOM Force CT scanner using dual-energy CT imaging protocols. Both CT scanners apply the dual-source strategy for dual-energy data acquisition. The protocols of the patient data acquisition are listed in Table II.

2.E. Evaluation

We compared the performance of the proposed method with those using the direct inversion.^{1,2} To further evaluate the performance of the proposed method, we also apply a classical separate low-pass filtration method^{35,36} to suppress the high noise in the direct decomposition.^{1,2}

The noise is quantitatively measured using STD of the image pixels within a uniform region of interest (ROI), and it is defined as

$$\text{STD} = \sqrt{\frac{1}{M} \sum_{m=1}^M (x_{lm} - \bar{x}_l)^2}, \quad (28)$$

where m is the pixel index within the ROI, x_{lm} is the value of each pixel of the ROI for the l -th material image, \bar{x}_l is the mean of the ROI for the material image, and M is the total number of pixels in the selected ROI.

The volume fraction accuracy of L_0 material study is quantified as

$$\text{VF} = \left(1 - \frac{1}{L_0} \sum_{l=1}^{L_0} \frac{\|x_l^{\text{truth}} - \bar{x}_l\|}{x_l^{\text{truth}}} \right) \times 100\%, \quad (29)$$

where x_l^{truth} and \bar{x}_l are the ground truth and decomposition result of the volume fraction for the l -th material image, respectively. L_0 is the total number of materials.

To investigate the image quality at the same noise level using different algorithms, a uniform area in the decomposed images is selected as the region of interest (ROI), and noise power spectrum (NPS) is applied as a metric to evaluate the image quality. The 2D NPS is defined as

$$\text{NPS} \approx |DFT_2\{f\}|^2, \quad (30)$$

where f denotes the ROI in which gray values are offset to achieve a zero mean, $DFT_2\{f\}$ is the 2D Discrete Fourier Transform (DFT) on f .³⁷

To evaluate the spatial resolution of decomposition results, the modulation transfer function (MTF)³⁸ is calculated on the digital and Catphan©600 phantoms. The MTF is obtained using the Fourier transform on the line spread function (LSF), which is the gradient of object edge profile. In addition, to minimize the fluctuation due to image noise, the resultant MTF is calculated from the average profile of adjacent boundaries of object. The measured frequencies at MTF magnitude decreased to 0.5 (−3 dB) are compared to evaluate the relative spatial resolution.³⁹

In the Catphan©600 phantom study, the decomposition accuracy is further evaluated using the electron density. The electron density is calculated as:⁴

$$\vec{\rho}_e = \sum_{l=1}^{L_0} \rho_l \vec{x}_l, \quad (31)$$

where \vec{x}_l and ρ_l are volume fraction and electron density of the l -th basis material, respectively. L_0 is the total number of materials. In each rod, the average percentage error of electron density is calculated as

TABLE II. Data acquisition parameters applied in patient data acquisition.

Body part	Pelvis	Head	Thigh
Scanner	Siemens SOMATOM Definition flash CT	Siemens SOMATOM Definition flash CT	Siemens SOMATOM Force CT
High-energy CT image			
Peak voltage (kVp)	140	140	150
X-ray Tube Current (mA)	146	364	97
Exposure Time(s)	0.500	0.285	0.500
Current-exposure Time Product (mAs)	73.0	103.7	48.5
Noise STD (mm ⁻¹)	4.09e-04	1.57e-04	3.43e-04
Helical Pitch	0.7	0.7	0.7
Gantry Rotation Speed (circle/second)	0.28	0.28	0.25
Low-energy CT image			
Peak voltage (kVp)	100	80	80
X-ray Tube Current (mA)	186	648	148
Exposure Time(s)	0.500	0.285	0.500
Current-exposure Time Product (mAs)	93.0	184.7	74.0
Noise STD (mm ⁻¹)	7.27e-04	3.61e-04	4.48e-04
Helical Pitch	0.7	0.7	0.7
Gantry Rotation Speed (circle/second)	0.28	0.28	0.25

$$E(\%) = \left(\frac{|\bar{\rho}_e - \rho_e^{truth}|}{\rho_e^{truth}} \right) \times 100\%, \quad (32)$$

where $\bar{\rho}_e$ is the average electron density inside one rod, ρ_e^{truth} is the ground truth of electron density in the corresponding rod. The root-mean-square percentage errors RMSE(%) of all the rods are summarized to quantify the decomposition accuracy of electron density.

3. RESULTS

3.A. Digital phantom study

The digital phantom consists of four types of area as shown in Fig. 1(a). The background is fat and labeled as #1, the bone is labeled as #2, and the muscle is labeled as #3. To better evaluate the decomposition performance, mixed materials are included within one pixel and the area is labeled as #4. Area #4 consists of fat and muscle, and the proportion of fat to muscle is 3:7.

We select bone, fat, muscle, and air as the basis materials. The decomposed basis material images are shown from the 1st to the 4th column in Fig. 2. The 1st row shows the results using direct inversion without noise suppression. The 2nd row shows the results using low-pass filtration method. The 3rd row shows the results using the proposed method. For fair comparison, the decomposition results of the low-pass filtration and the proposed methods are compared at the comparable noise STD. The proposed method successfully differentiates basis materials and suppresses the high noise STD in the direct decomposition results.

For quantitative analysis, several ROIs located within the uniform area of the basis materials are selected in the dashed

circles of Fig. 1(b). The means and noise STDs of the decomposed basis material images are summarized in Table III. The volume fraction accuracies are 82.42%, 92.43%, and 93.77% using the direct inversion, the low-pass filtration, and the proposed method, respectively. The proposed method improves the volume fraction accuracy by 11.35% compared with the direct inversion. In addition, the proposed method successfully differentiates the mixed materials within one pixel. In ROI3 where fat and muscle are mixed, the proposed method increases the volume fraction accuracy by 24.66% as compared with the direct inversion method.

The image quality of the low-pass filtration is worse than that using the proposed method despite the comparable noise STD. The major reason is that noise correlation is included into the proposed scheme. To take a deep look into the frequency characteristics, the NPS is measured within an ROI of 200 by 200 pixels centered in the decomposed fat image, and the result is shown in Fig. 3. The low-pass filtration method removes the textures in the decomposed results due to its strong and uncorrelated noise suppression.

To evaluate the capability of spatial resolution maintenance, the typical MTFs of muscle and mixture are plotted in Fig. 4. Compared with the low-pass filtration method, the proposed method increases the spatial resolution by an overall factor of 1.64 at MTF magnitude decreased to 50%.

3.B. Catphan©600 phantom study

The proposed method is evaluated using a contrast rod slice of the Catphan©600 phantom. The low- and high-energy CT images are shown in Fig. 5.

In this study, we insert iodine solutions with different concentrations into the phantom, whose nominal concentrations are 10 mg/ml and 5 mg/ml, respectively. The rods in this

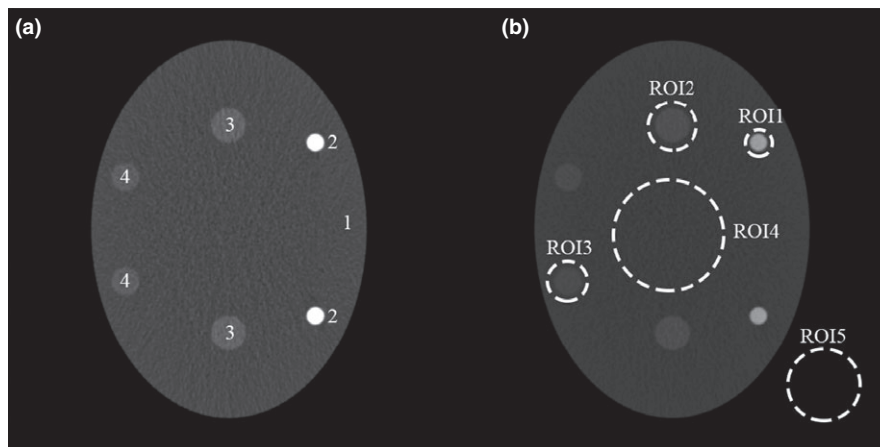


FIG. 1. CT images of the digital phantom: (a) The low-energy: 75 kVp and (b) The high-energy: 140 kVp. Display window is $[0.01\ 0.04]\ \text{mm}^{-1}$. The components of ROIs are bone (ROI1), muscle (ROI2), mixture (ROI3), fat (ROI4), and air (ROI5), respectively.

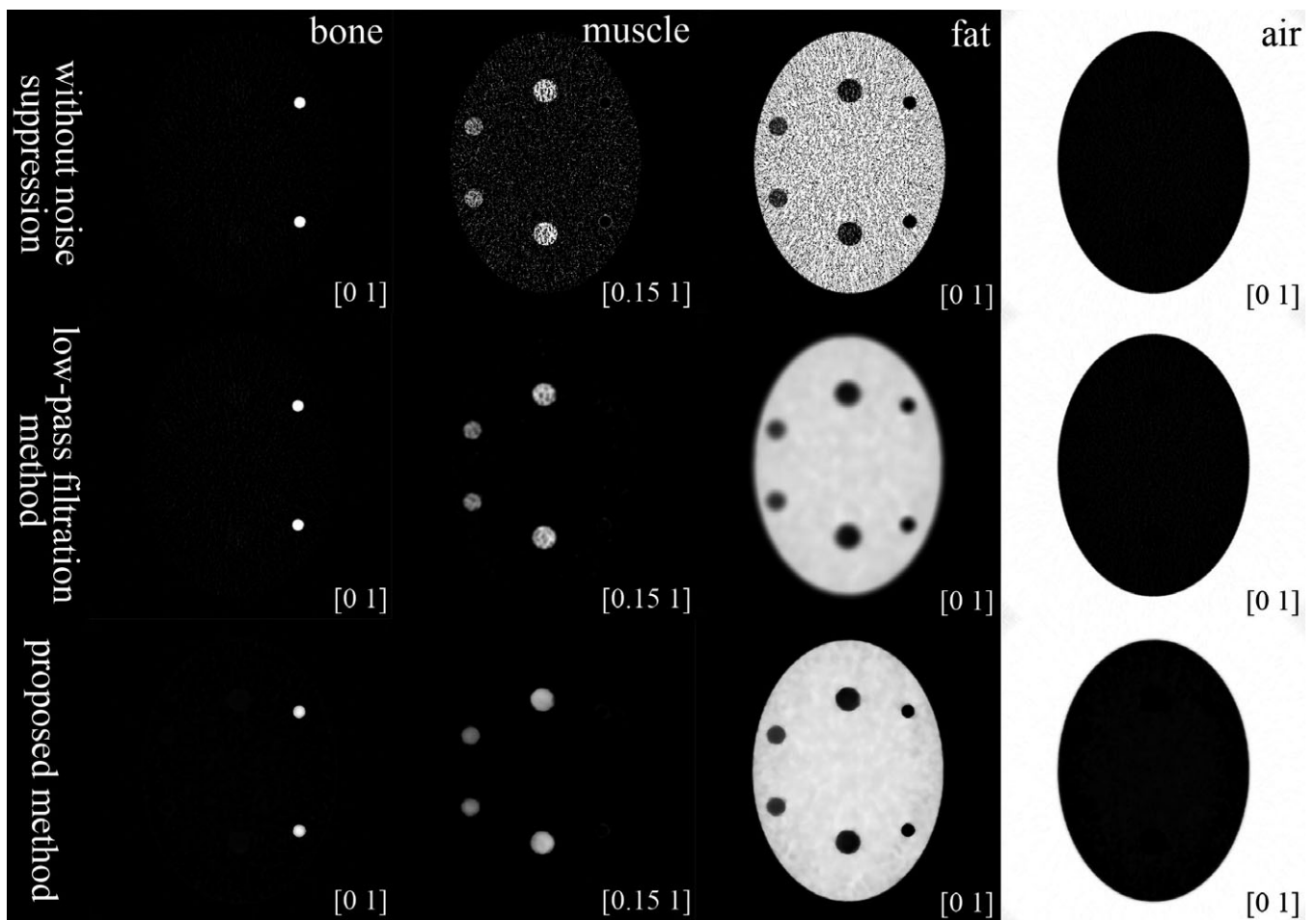


FIG. 2. The decomposed bone (the 1st column), muscle (the 2nd column), fat (the 3rd column), and air (the 4th column) images of the digital phantom. Display windows are shown in the bottom-right corner.

slice are labeled in Fig. 5(a): Teflon (labeled as #1), Delrin (labeled as #2), Iodine solution of 10 mg/ml (labeled as #3), Polystyrene (labeled as #4), low-density Polyethylene (LDPE) (labeled as #5), Polymethylpentene (PMP) (labeled as #6), Iodine solution of 5 mg/ml (labeled as #7). We select Teflon

(ROI1), Delrin (ROI2), Iodine solution of 10 mg/ml (ROI3), PMP (ROI4), Inner soft tissue (ROI5), and Air (ROI6) as the basis materials. The decomposed basis material images are shown from the 1st to the 6th column in Fig. 6. The decomposition results using different methods are shown from the 1st

TABLE III. The means and STDs of decomposed images within each ROI.

Methods	ROI1 Bone	ROI2 Muscle	ROI3		ROI4 Fat	ROI5 Air
			Muscle	Fat		
Ground truth	1.000	1.000	0.700	0.300	1.000	1.000
W/o noise suppression	0.9760 ± 0.0089	0.7282 ± 0.2614	0.5366 ± 0.2660	0.4047 ± 0.2517	0.8262 ± 0.2319	0.9970 ± 0.0041
Low-pass filtration	0.9760 ± 0.0089	0.7817 ± 0.0839	0.6557 ± 0.0405	0.3154 ± 0.0053	0.9058 ± 0.0091	0.9970 ± 0.0041
Proposed method	0.9774 ± 0.0040	0.8103 ± 0.0239	0.6697 ± 0.0104	0.3138 ± 0.0050	0.9308 ± 0.0084	0.9973 ± 0.0036

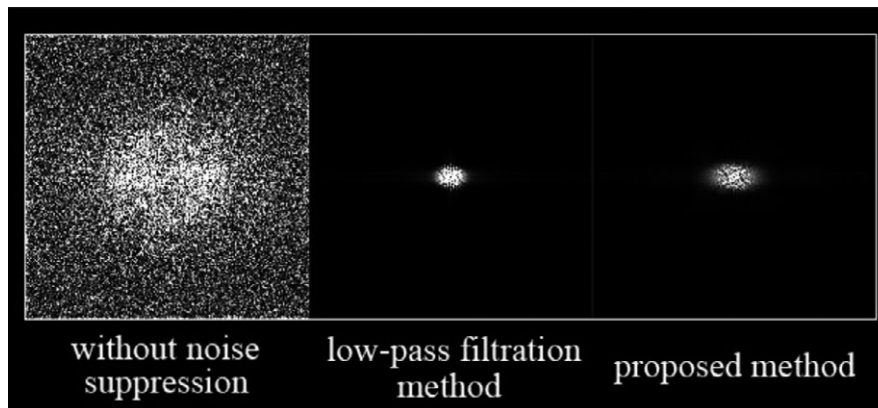


FIG. 3. Measured NPS on the decomposed fat image generated using different methods. The display windows is [0 4000].

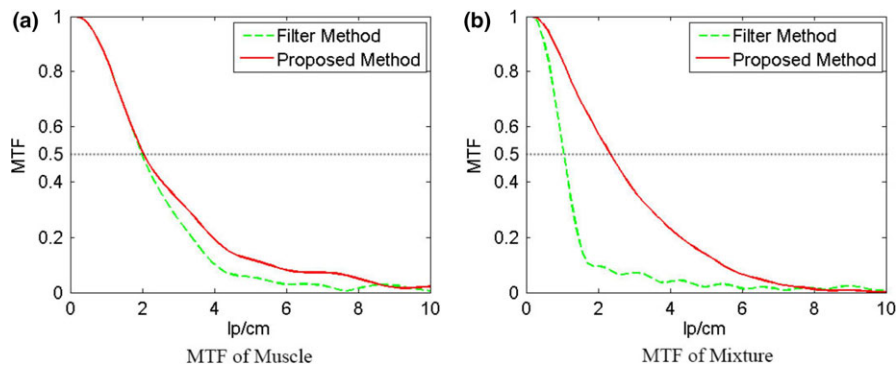


FIG. 4. MTF curves measured on the muscle and mixture areas [Colour figure can be viewed at wileyonlinelibrary.com]

to the 3rd row. The enlarged views of corresponding material images highlighted with white dashed boxes from the 1st to the 4th column are shown in the bottom-left corner. The proposed method successfully differentiates basis materials and suppresses the high noise STD in the direct decomposition. In addition, the iodine solution is infused into plastic bottles, whose linear attenuation coefficient is close to PMP. In the decomposed results, the proposed method still distinguishes them from those in the PMP image.

For quantitative analysis, the means and noise STDs of the decomposed basis material images within the ROIs shown in Fig. 5(b) are summarized in Table IV. The volume fraction accuracies using the three methods (direction inversion, low-pass filtration, and the proposed) are 68.62%, 66.16%, and 79.35%, respectively. The proposed method improves the

volume fraction accuracy by 10.73% and 13.19% as compared with the direct inversion and low-pass filtration method, respectively.

The estimated average electron densities and the RMSE (%) for different contrast rod materials are summarized in Table V. The RMSE(%) is 32.70% in the low-pass filtration method, and decreased to 11.81% in the proposed method. The proposed method achieves the balance between high image quality and strong noise suppression.

To take a deep look into the frequency characteristics, the NPS is measured within an ROI of 160 by 160 pixels centered in the decomposed soft tissue image, and the result is shown in Fig. 7. The low-pass filtration method removes the texture of decomposed results with strong noise suppression.

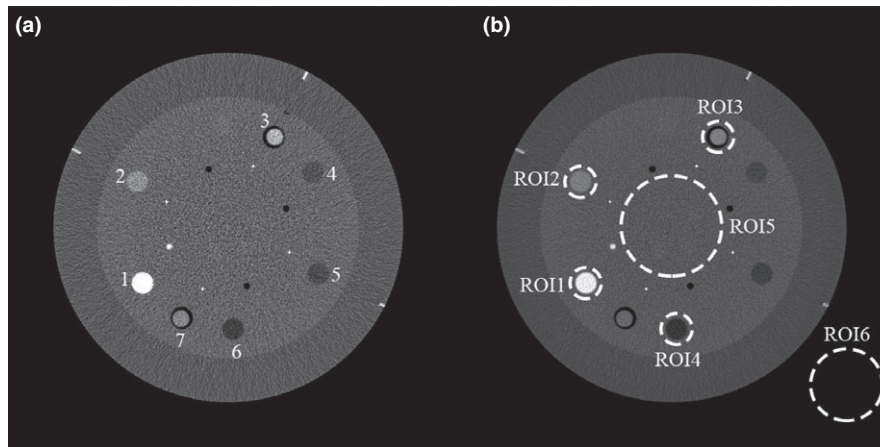


FIG. 5. CT images of the Catphan©600 phantom on the contrast rods slice: (a) The low-energy: 75 kVp and (b) The high-energy: 125 kVp. Display window is $[0.01 \ 0.04] \text{ mm}^{-1}$. The components of ROIs are Teflon (ROI1), Delrin (ROI2), Iodine solution of 10 mg/ml (ROI3), PMP (ROI4), Inner soft tissue (ROI5), and Air (ROI6), respectively.

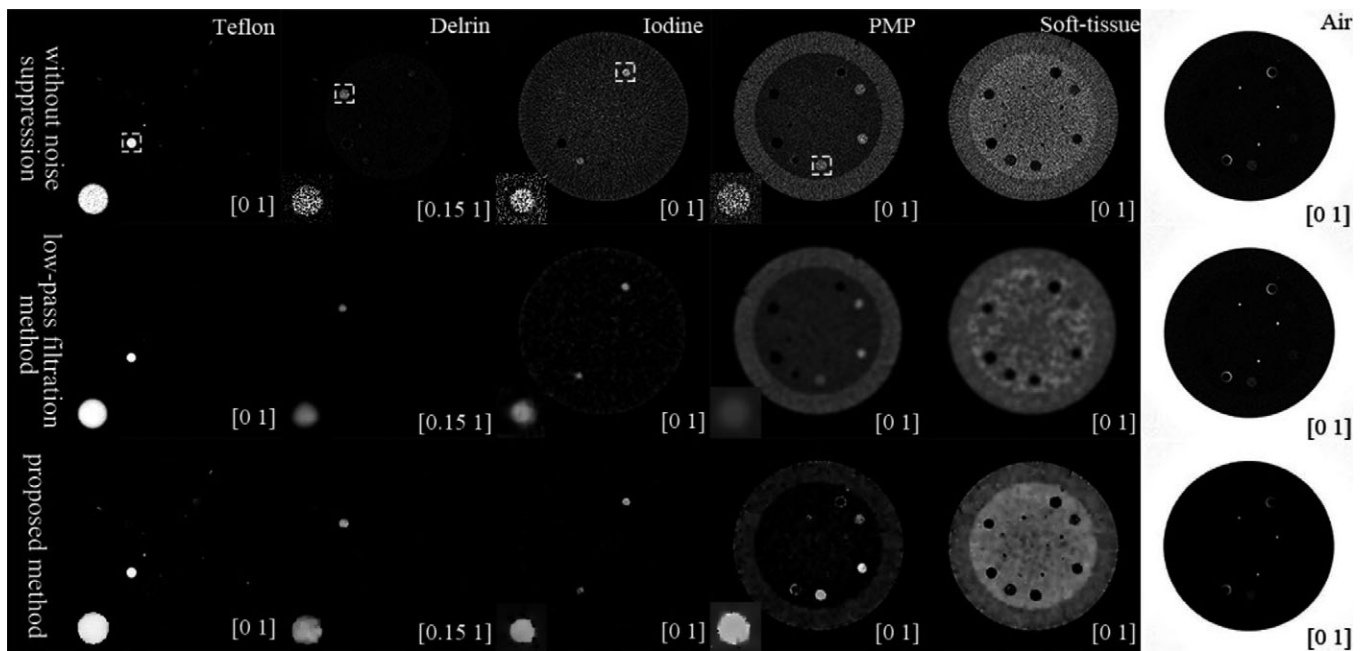


FIG. 6. The decomposed Teflon (the 1st column), Delran (the 2nd column), Iodine (the 3rd column), PMP (the 4th column), Soft tissue (the 5th column), and Air (the 6th column) images of the Catphan©600 phantom on the contrast rods slice. The display windows are shown in the bottom-right corner of the subfigures.

TABLE IV. The means and STDs of decomposed images within each ROI.

Methods	ROI1 Teflon	ROI2 Delran	ROI3 Iodine	ROI4 PMP	ROI5 Soft tissue	ROI6 Air
W/o noise suppression	0.9578 ± 0.0642	0.5852 ± 0.3340	0.6190 ± 0.3290	0.5067 ± 0.3088	0.4493 ± 0.3236	0.9995 ± 0.0037
Low-pass filtration	0.9578 ± 0.0642	0.6089 ± 0.0504	0.6346 ± 0.0475	0.3676 ± 0.0078	0.4015 ± 0.0398	0.9994 ± 0.0023
Proposed method	0.9615 ± 0.0043	0.7306 ± 0.0367	0.7112 ± 0.0188	0.7788 ± 0.0071	0.5790 ± 0.0388	0.9999 ± 0.0018

To evaluate the capability of spatial resolution retaining, the typical MTFs of iodine solution (10 mg/ml) and PMP are plotted in Fig. 8. Compared with the low-pass filtration

method, the proposed method increases spatial resolution by an overall factor of 2.16 at MTF magnitude decreased to 50%.

TABLE V. Electron densities inside the Catphan©600 contrast rods. The numbers of the rods are marked in Fig. 5(a). The last column is RMSE(%) of the seven rods. The electron density of iodine solutions is calculated based on iodine concentrations. The unit of the electron density is 10^{23} e/cm^3 .

Rods	1 Teflon	2 Delrin	3 Iodine solution (10 mg/ml)	4 Polystyrene	5 LDPE	6 PMP	7 Iodine solution (5 mg/ml)	RMSE(%)
Ground truth	6.240	4.525	3.368	3.400	3.155	2.851	3.356	
W/o noise suppression	6.158	4.127	3.882	2.984	2.729	2.274	3.370	
Average Percentage Errors E(%)	1.31%	8.80%	15.26%	12.24%	13.50%	20.24%	0.42%	12.27%
Low-pass filtration	5.999	3.318	3.025	2.716	1.809	1.232	2.190	
Average Percentage Errors E(%)	3.86%	26.67%	10.18%	20.12%	42.66%	56.79%	34.74%	32.70%
Proposed method	6.171	4.288	3.936	3.140	2.769	2.243	3.348	
Average Percentage Errors E(%)	1.11%	5.24%	16.86%	7.65%	12.23%	21.33%	0.24%	11.81%

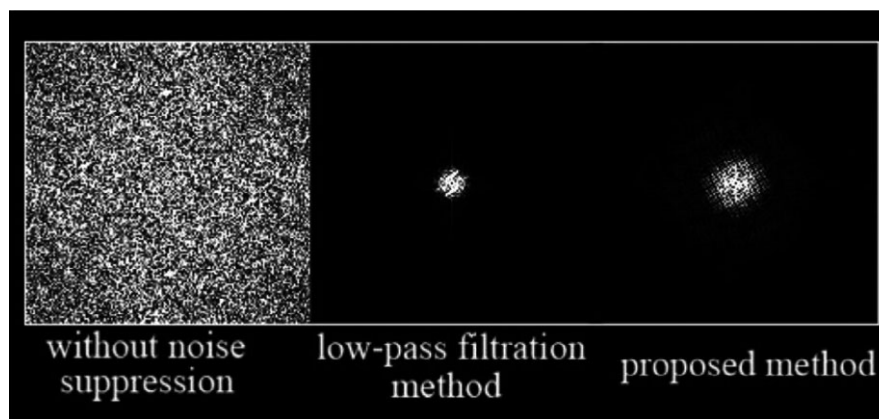


FIG. 7. Measured NPS on the decomposed soft tissue image generated using different methods. The display windows: [0 4000].

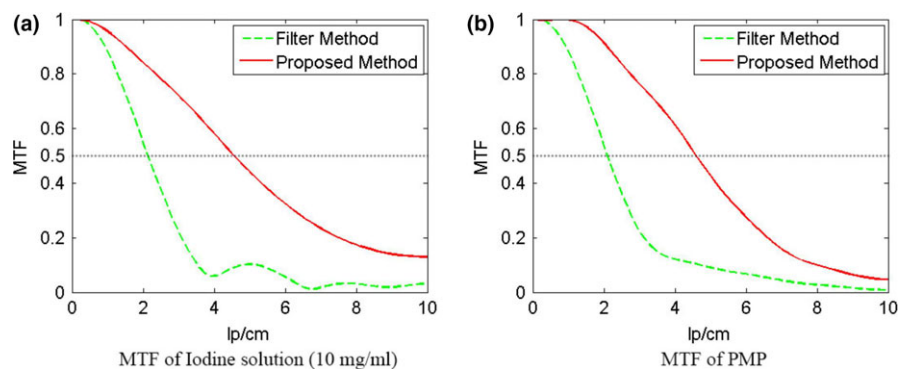


FIG. 8. MTF curves measured on iodine solution (10 mg/ml) and PMP areas. [Colour figure can be viewed at wileyonlinelibrary.com]

3.C. Patient Studies

The proposed method is also evaluated using the clinical data.

3.C.1. Pelvis study

The CT images of pelvis patient are shown in Fig. 9.

The bone, iodine, muscle, fat, and air are selected as the basis materials. And the decomposed basis material images are shown from the 1st to the 5th column in Fig. 10. The decomposition results using different methods are shown

from the 1st to the 3rd row. The proposed method successfully differentiates basis materials and suppresses the high noise STD in the direct decomposition.

For quantitative analysis, the means and noise STDs in the ROIs of the decomposed basis material images shown in Fig. 9(b) are summarized in Table VI. The volume fraction accuracies using the three methods (direction inversion, low-pass filtration, and the proposed) are 77.59%, 72.06%, and 86.29%, respectively. The proposed method improves the volume fraction accuracy by 8.70% and 14.23% compared with the direct inversion and low-pass filtration method, respectively.

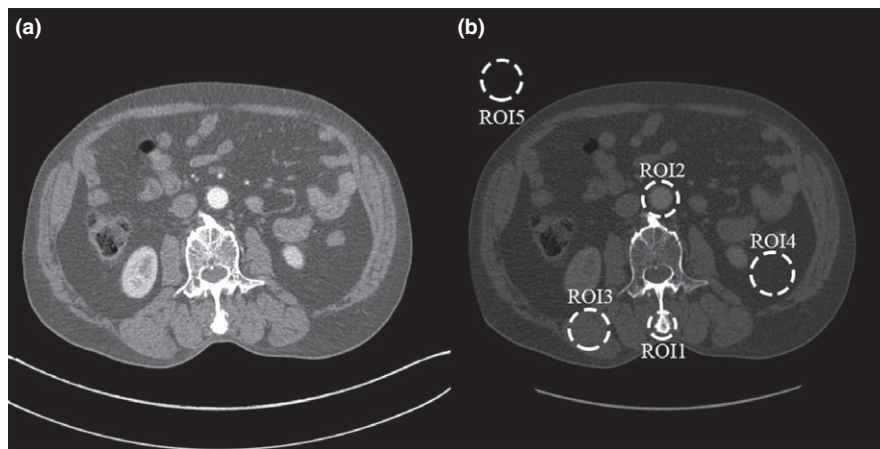


FIG. 9. CT images of a pelvis patient. (a) The low-energy: 100 kVp and (b) The high-energy: 140 kVp. Display window is $[0.012 \ 0.032] \text{ mm}^{-1}$. The major components of ROIs are bone (ROI1), iodine solution (ROI2), muscle (ROI3), fat (ROI4), and air (ROI5), respectively.

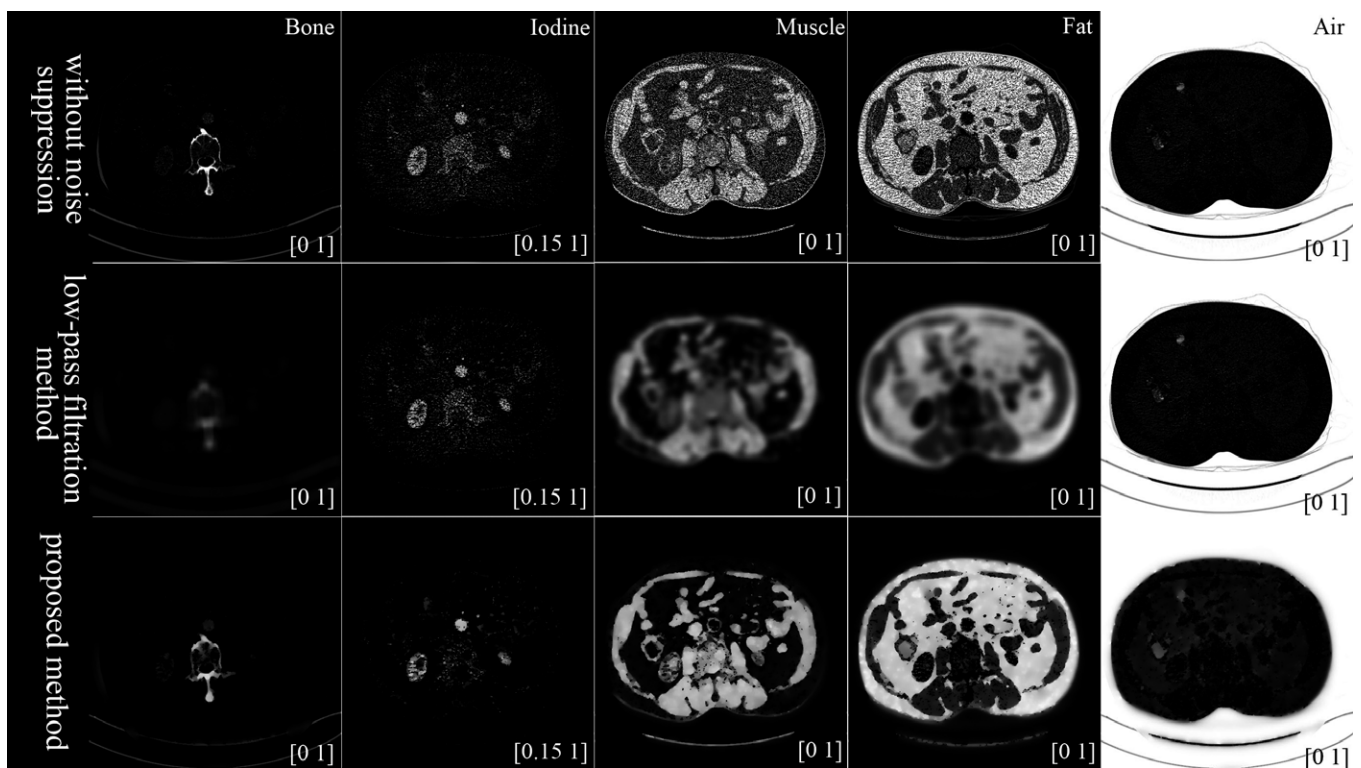


FIG. 10. The decomposed bone (the 1st column), iodine (the 2nd column), muscle (the 3rd column), fat (the 4th column), and air (the 5th column) images. The display windows are shown in the bottom-right corner.

The NPS is measured within an ROI of 100 by 100 pixels in the decomposed fat image, and the result is shown in Fig. 11. The low-pass filtration method removes the texture of decomposed results with strong noise suppression, while the proposed method still retains the texture information due to the correlated noise suppression scheme.

3.C.2. Head study

The CT images of the head patient are shown in Fig. 12.

The bone, iodine, muscle, fat, and air are selected as the basis materials, and the decomposed basis material images are shown in Fig. 13. The proposed method successfully differentiates basis materials and suppresses the high noise STD in the direct decomposition. In addition, the areas pointed by the red arrows are parotid glands, whose linear attenuation coefficient is between fat and muscle. In Fig. 13, the proposed method successfully differentiates these areas, while retaining the spatial resolution of decomposition results.

For quantitative analysis, the means and noise STDs of the decomposed basis material images within the ROIs shown in

TABLE VI. The means and STDs of decomposed images within each ROI.

Methods	ROI1 Bone	ROI2 Iodine	ROI3 Muscle	ROI4 Fat	ROI5 Air
W/o noise suppression	0.8652 ± 0.1248	0.6282 ± 0.2781	0.6623 ± 0.2603	0.7237 ± 0.2711	1.0000 ± 0.0000
Low-pass filtration	0.4916 ± 0.0159	0.6524 ± 0.1867	0.6888 ± 0.0272	0.7703 ± 0.0225	1.0000 ± 0.0000
Proposed method	0.8806 ± 0.0056	0.7801 ± 0.1681	0.7914 ± 0.0194	0.8623 ± 0.0208	1.0000 ± 0.0000

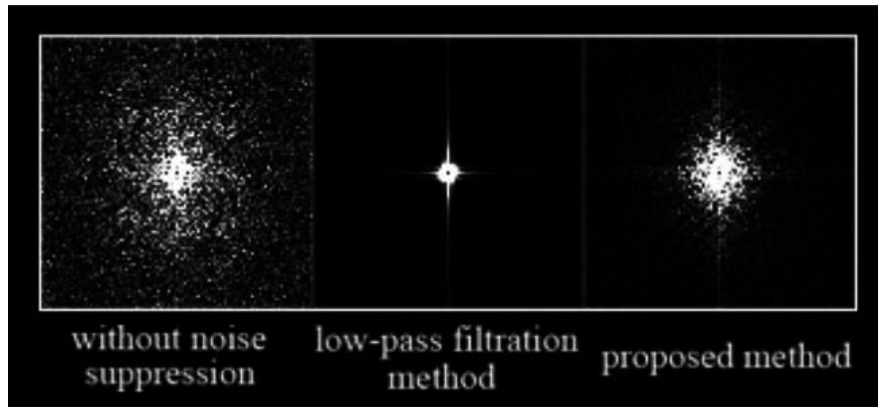


FIG. 11. Measured NPS on the decomposed fat image generated using different methods. The display windows: [0 2500].

Fig. 12(b) are summarized in Table VII. The volume fraction accuracies using the three methods (direction inversion, low-pass filtration, and the proposed) are 92.99%, 92.80%, and 94.13%, respectively.

3.C.3. Thigh study

The CT images of the thigh patient are shown in Fig. 14.

The bone, muscle, fat, and air are selected as the basis materials, and the decomposed basis material images are shown in Fig. 15. The proposed method successfully differentiates basis materials and suppresses the high noise STD in the direct decomposition. In addition, the areas pointed by the red arrows are bone marrow and connective fiber, whose linear attenuation coefficients are between those of fat and muscle. In Fig. 15, the proposed method successfully differentiates these areas, while retaining the spatial resolution of decomposition results.

For quantitative analysis, the means and noise STDs of the decomposed basis material images within the ROIs shown in Fig. 14(b) are summarized in Table VIII. The volume fraction accuracies using the three methods (direction inversion, low-pass filtration, and the proposed) are 91.09%, 92.80%, and 93.44%, respectively.

3.D. Implementation details

In the implementations, we initialized the proposed method using results of the direct inversion method. And the statistical weight V_p is normalized as $V_p = \text{diag}(\text{var}(\mu_{Hp})/\text{var}(\mu_{Lp}), 1)$. The threshold of the stopping criterion is set as $1.0e-05$. The cost function of the

proposed method has two tunable parameters. The parameter beta controls the noise resolution, while delta controls the edge preservation. For different materials, the decomposed image contains different content, and the situations of neighbored pixels are also different. Therefore, we empirically selected the optimal combination of these parameters to balance the noise suppression and spatial resolution maintenance. Table IX listed the regularization coefficients β_i , and the edge-preserving parameters δ_i for each material in every study.

4. DISCUSSION

We proposed a statistical image-domain MMD method for DECT. As in previous work,¹⁻³ we applied mass and volume conservation constraints and the assumptions that each pixel contains at most three materials and material triplets vary among pixels to decrease the degrees of freedom to two per pixel for a given triplet so that reconstructing multi-material images from DECT measurement is feasible. The cost function is in the form of PWLS reconstruction with a negative log-likelihood term and edge-preserving regularization for each material image. The statistical weight is determined by a data-based method accounting for the noise variance of high- and low-energy CT images. We applied the optimization transfer principles to design a series of pixel-wise separable quadratic surrogates (PWSQS) functions which monotonically decrease the cost function.³ As the surrogates are pixel-wise separable, the proposed method can update all pixels simultaneously, which allows faster convergence. Since the cost function in Eq. (12) under constraints in

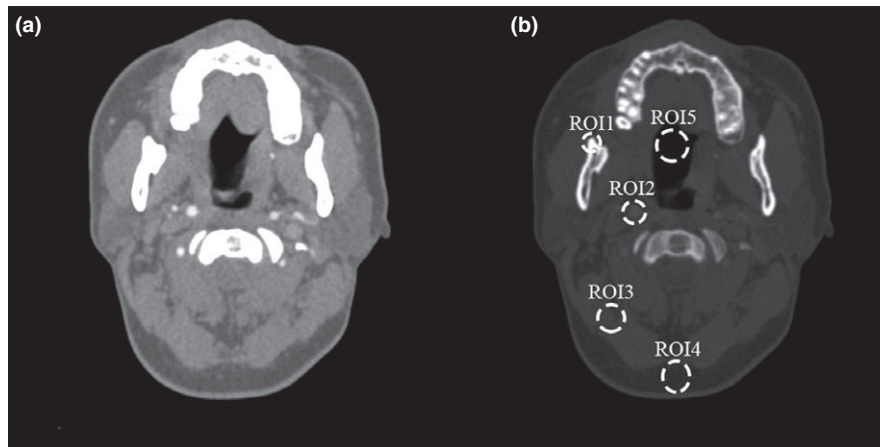


FIG. 12. CT images of a head patient. (a) The low-energy: 80 kVp and (b) The high-energy: 140 kVp. Display window is $[0.01 \ 0.035] \text{ mm}^{-1}$. The major components of ROIs are bone (ROI1), iodine solution (ROI2), muscle (ROI3), fat (ROI4), and air (ROI5), respectively.

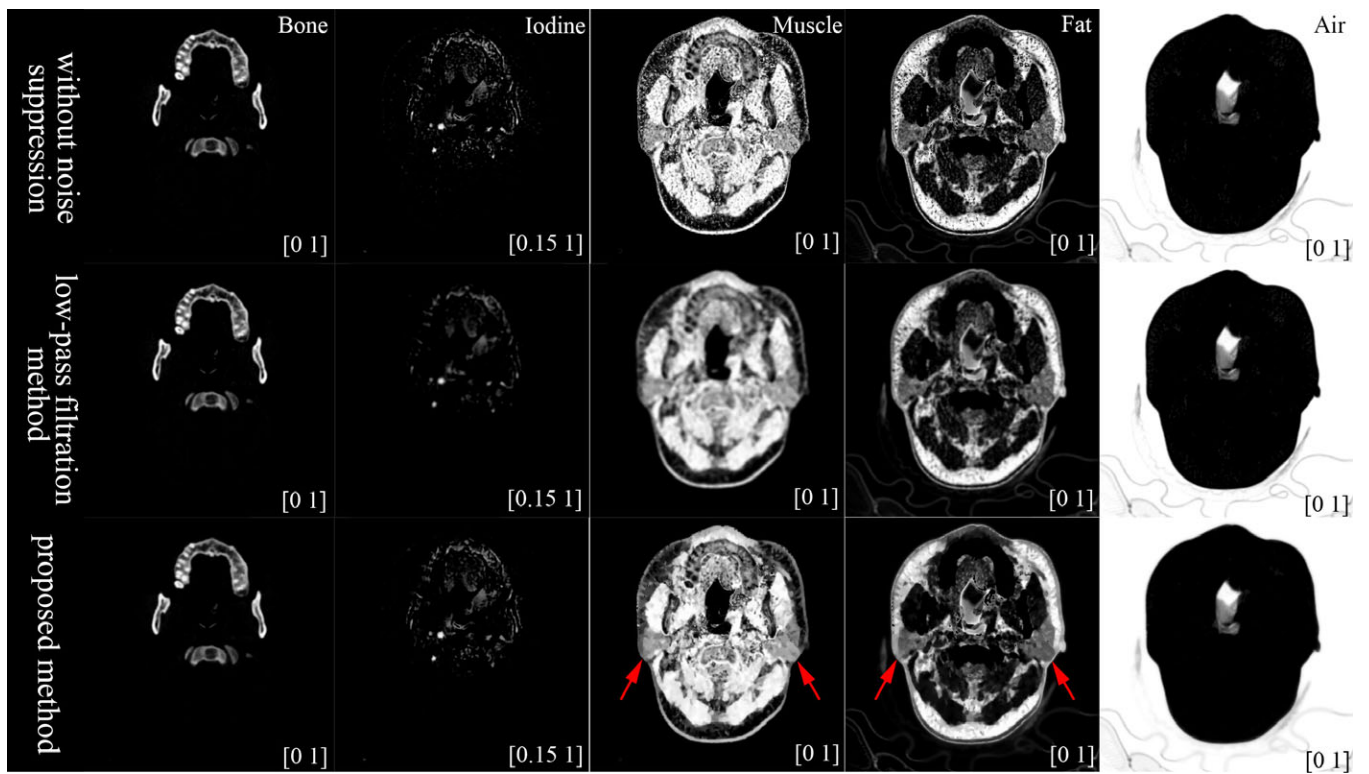


FIG. 13. The decomposed bone (the 1st column), iodine (the 2nd column), muscle (the 3rd column), fat (the 4th column), and air (the 5th column) images. The display windows are shown in the bottom-right corner. [Colour figure can be viewed at wileyonlinelibrary.com]

TABLE VII. The means and STDs of decomposed images within each ROI.

Methods	ROI1 Bone	ROI2 Iodine	ROI3 Muscle	ROI4 Fat	ROI5 Air
W/o noise suppression	0.9719 ± 0.0556	0.9056 ± 0.0656	0.9382 ± 0.0733	0.8602 ± 0.1465	0.9735 ± 0.0226
Low-pass filtration	0.9713 ± 0.0554	0.8700 ± 0.0572	0.9573 ± 0.0210	0.8679 ± 0.0863	0.9735 ± 0.0226
Proposed method	0.9722 ± 0.0524	0.9135 ± 0.0540	0.9575 ± 0.0161	0.8898 ± 0.0843	0.9737 ± 0.0222

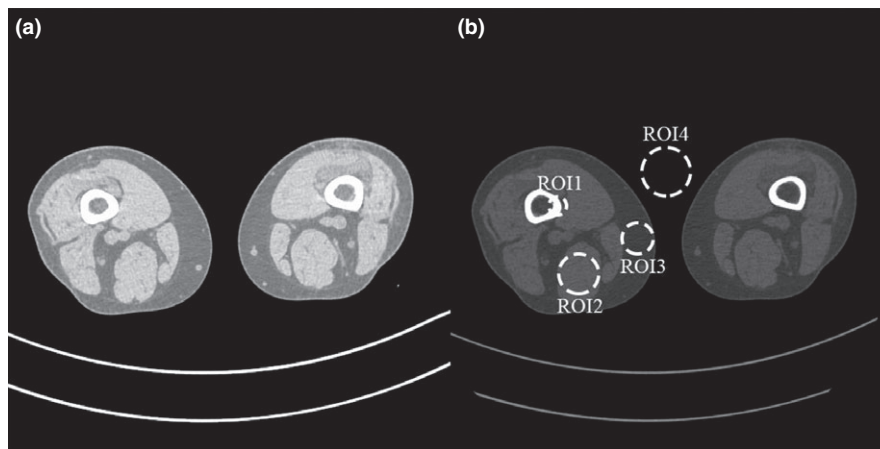


FIG. 14. CT images of a thigh patient. (a) The low-energy: 80 kVp and (b) The high-energy: 150 kVp. Display window is $[0.012\ 0.032]\ \text{mm}^{-1}$. The major components of ROIs are bone (ROI1), muscle (ROI2), fat (ROI3), and air (ROI4), respectively.

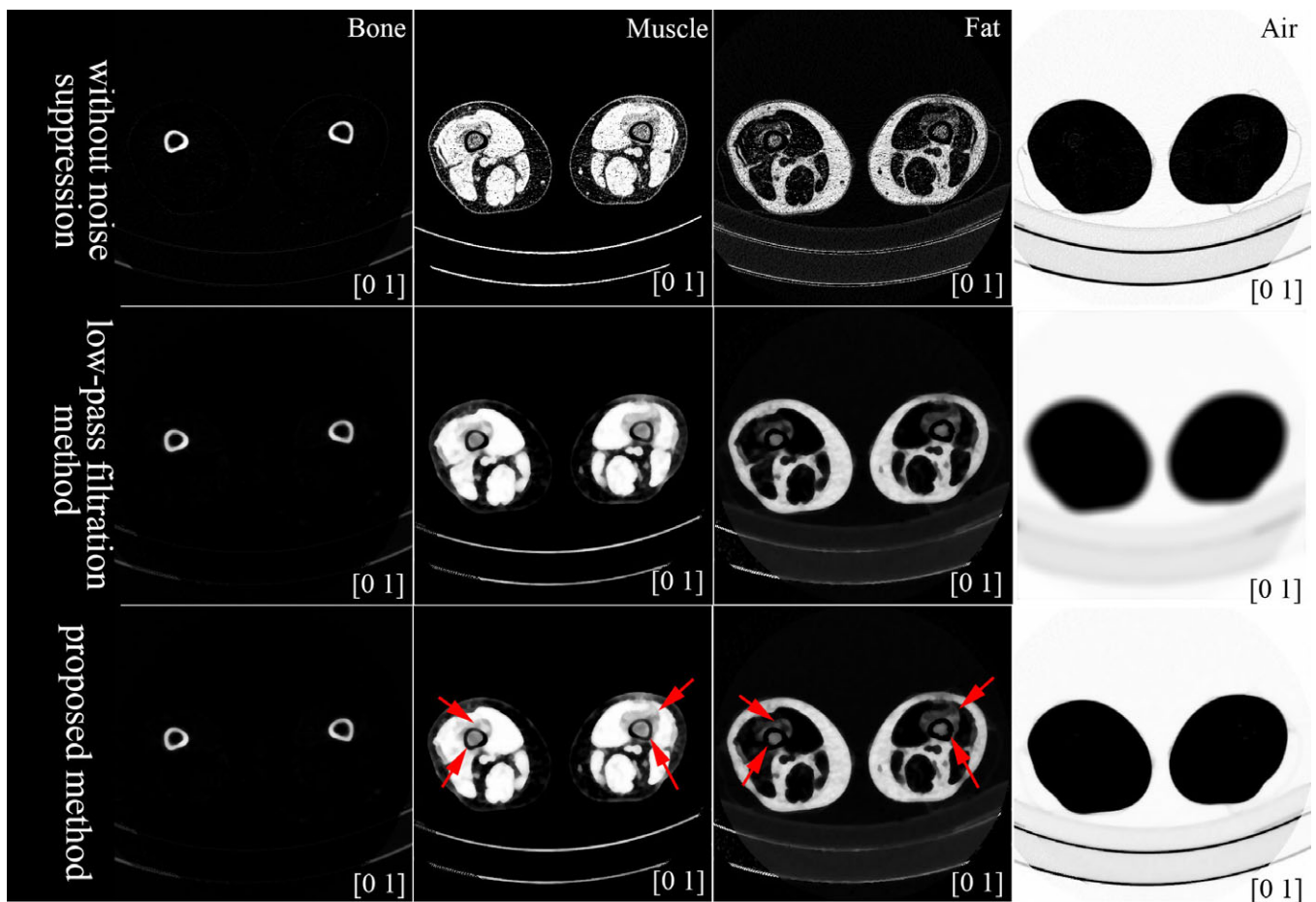


FIG. 15. The decomposed bone (the 1st column), muscle (the 2nd column), fat (the 3rd column), and air (the 4th column) images. The display windows are shown in the bottom-right corner. [Colour figure can be viewed at wileyonlinelibrary.com]

Eqs. (2)–(4) is nonconvex, a good initialization is important to guarantee convergence to a decent local minimum. We initialized the proposed method using results of the direct inversion method. The proposed method is a practical image-domain method where CT images at low and high energies are modeled as weighted linear combinations

of linear attenuation coefficients of basis materials with weights beginning their volume fractions. The proposed method incorporates noise variance of DECT images into statistical weight in PWLS estimation, which effectively overcomes the issue of magnified noise in the decomposed basis materials by the direct inversion method.^{1,2}

TABLE VIII. The means and STDs of decomposed images within each ROI.

Methods	ROI1 Bone	ROI2 Muscle	ROI3 Fat	ROI4 Air
W/o noise suppression	0.9099 ± 0.0820	0.9451 ± 0.1189	0.8086 ± 0.1496	0.9801 ± 0.0091
Low-pass filtration	0.9091 ± 0.0379	0.9804 ± 0.0229	0.8427 ± 0.0400	0.9799 ± 0.0021
Proposed method	0.9270 ± 0.0353	0.9844 ± 0.0199	0.8455 ± 0.0311	0.9806 ± 0.0020

TABLE IX. The regularization coefficients and edge-preserving parameters for each study.

Data	β_l	δ_l
Digital phantom (for bone, muscle, fat, and air images)	0.01, 0.01, 0.1, 0.01	0.1, 0.1, 0.01, 0.1
Catphan©600 phantom (for teflon, delrin, iodine, PMP, soft tissue, and air images)	0.6, 5, 2.5, 1, 1, 7	0.005, 0.005, 0.02, 0.012, 0.012, 0.012
Pelvis patient data (for bone, iodine, muscle, fat, and air images)	1, 1.5, 0.9, 0.9, 0.1	0.01, 0.005, 0.01, 0.01, 0.1
Head patient data (for bone, iodine, muscle, fat, and air images)	0.2, 0.3, 0.09, 0.09, 0.04	0.01, 0.005, 0.01, 0.01, 0.1
Thigh patient data (for bone, muscle, fat, and air images)	0.03, 0.01, 0.05, 0.09	0.05, 0.08, 0.01, 0.01

The cost function of the proposed method has two tunable parameters (i.e., regularization coefficient and edge-preserving coefficient). The choice of parameters for one basis material image influences the decomposed images of other components. An appropriate combination of parameters needs to be carefully determined for each application. We empirically selected the optimal combination of these parameters to balance the noise suppression and spatial resolution maintenance. Determining tunable parameters remains a challenge for the proposed method, just as that for other methods with multiple parameters. In the future, we will further investigate optimal selection of these parameters using material-cross penalty, such as total nuclear variation (TNV).⁴⁰

In the current implementation, we assumed uniform distribution of noise variance map in DECT images, and measured the noise variance inside a manually selected region of homogeneous material. The performance of the proposed method can be further improved by substituting the uniform noise variance map with a pixel-dependent one. Several analytic algorithms are proposed in literature to calculate the noise variance for DECT images. Wunderlich and Noo presented a method for computing image variance.⁴¹ Li et al. proposed a computationally efficient technique for noise estimation directly from CT images.⁴² A forward projection, based on a 2D fan-beam approximation, was used to generate the projection data, with a noise model incorporating the effects of the bowtie filter and automatic exposure control. The noise propagation from projection data to images was analytically derived. In future work, we will combine noise variance estimation with the proposed decomposition method, and evaluate its performance on clinical applications. In addition, we will conduct more studies on the clinical data to fully evaluate the efficacy of the proposed method.

5. CONCLUSIONS

We proposed a statistical image-domain MMD method using DECT measurements. The proposed method applies extra constraints of volume and mass conservation and the assumptions that at most three materials in each pixel and various material types among pixels. The proposed multimaterial images are faithfully decomposed from the dual-energy measurements. It is thus practical to be implemented in clinical applications.

ACKNOWLEDGMENTS

The work was supported by the Zhejiang Provincial Natural Science Foundation of China (Grant No. LR16F010001), National High-tech R&D Program for Young Scientists by the Ministry of Science and Technology of China (863 Program, 2015AA020917), Natural Science Foundation of China (NSFC Grant No. 81201091, 51305257), National Key Research Plan by the Ministry of Science and Technology of China (Grant No. 2016YFC0104507) and Key Laboratory of Diagnosis and Treatment of Neonatal Diseases of Zhejiang Province (2016-ZJKD-ND-004). Yong Long was partially supported by NSFC (61501292), Shanghai Pujiang Talent Program (15PJ1403900), SJTU-UM Collaborative Research Program and Returned Overseas Chinese Scholars Program. Yu Kuang was supported in part by an NIH/NIGMS grant (P20GM103440).

CONFLICT OF INTEREST

The authors declare that they do not have any conflict of interest.

^{a)} Author to whom correspondence should be addressed. Electronic mails: tyniu@zju.edu.cn (Tianye Niu), and yong.long@sjtu.edu.cn (Yong Long).

REFERENCES

- Bhotika R, Thomsen B. Multi-material decomposition of spectral CT images. *Proc. SPIE*. 2010;7622:640–643.
- Mendonca PR, Lamb P, Sahani DV. A flexible method for multi-material decomposition of dual-energy CT images. *IEEE Trans Med Imaging*. 2014;33:99–116.
- Long Y, Fessler JA. Multi-material decomposition using statistical reconstruction for spectral CT. *IEEE Trans Med Imaging*. 2014;33:1614–1626.
- Niu T, Dong X, Petrongolo M, Zhu L. Iterative image-domain decomposition for dual-energy CT. *Med Phys*. 2014;41:041901.
- Alvarez RE, Macovski A. Energy-selective reconstructions in X-ray computerized tomography. *Phys Med Biol*. 1976;21:733–744.
- Alvarez RE, Macovski A. X-ray spectral decomposition imaging system. U.S. Patent 4 029 963 1977.
- Macovski A, Alvarez RE, Chan JL, Stonestrom JP, Zatz LM. Energy dependent reconstruction in X-ray computerized tomography. *Comput Biol Med*. 1976;6:325–336.
- Jr MW, Alvarez RE, Macovski A. Initial results with prereconstruction dual-energy computed tomography (PREDECT). *Radiology*. 1981;140:421–430.
- Stonestrom JP, Alvarez RE, Macovski A. A framework for spectral artifact corrections in x-ray CT. *IEEE Trans Biomed Eng*. 1981;28:128–141.
- Laidevant AD, Malkov S, Flowers CI, Kerlikowske K, Shepherd JA. Compositional breast imaging using a dual-energy mammography protocol. *Med Phys*. 2010;37:164–174.
- Liu X, Yu L, Primak AN, Mccollough CH. Quantitative imaging of element composition and mass fraction using dual-energy CT: Three-material decomposition. *Med Phys*. 2009;36:1602–1609.
- Huh W, Fessler JA. Model-based image reconstruction for dual-energy X-ray CT with fast KVP switching. *Proceedings*. 2009;326–329.
- Johnson T, Fink C, Schönberg SO, Reiser MF. Dual energy CT in clinical practice. *Med Phys*. 2011;38:6346–6346.
- Mccollough CH, Primak AN, Saba O, et al. Dose performance of a 64-channel dual-source CT scanner. *Radiology*. 2007;243:775–784.
- Petersilka M, Bruder H, Krauss B, Stierstorfer K, Flohr TG. Technical principles of dual source CT. *Eur J Radiol*. 2008;68:362–368.
- Rafecas M, Boning G, Pichler BJ, Lorenz E. A Monte Carlo study of high-resolution PET with granulated dual-layer detectors. *Nucl Sci IEEE Trans*. 2001;48:1490–1495.
- Foygel BR, Sidky EY, Gilat ST, Pan X. An algorithm for constrained one-step inversion of spectral CT data. *Phys Med Biol*. 2015;61:3784–3818.
- Sidky EY, Zou Y, Pan X. Impact of polychromatic x-ray sources on helical, cone-beam computed tomography and dual-energy methods. *Phys Med Biol*. 2004;49:2293–2303.
- Harms J, Wang T, Petrongolo M, Niu T, Zhu L. Noise suppression for dual-energy CT via penalized weighted least-square optimization with similarity-based regularization. *Med Phys*. 2016;43:2676–2686.
- Petrongolo M, Dong X, Zhu L. A general framework of noise suppression in material decomposition for dual-energy CT. *Med Phys*. 2015;42:2015.
- Zhang R, Thibault JB, Bouman C, Sauer K, Hsieh J. Model-based iterative reconstruction for dual-energy X-Ray CT using a joint quadratic likelihood model. *IEEE Trans Med Imaging*. 2013;33:117–134.
- De Pierro AR. A modified expectation maximization algorithm for penalized likelihood estimation in emission tomography. *IEEE Trans Med Imaging*. 1995;14:132–137.
- Erdoğan H, Fessler JA. Monotonic algorithms for transmission tomography. *IEEE Trans Med Imaging*. 1999;18:801–814.
- Jacobson MW, Fessler JA. An expanded theoretical treatment of iteration-dependent majorize-minimize algorithms. *IEEE Trans Image Process*. 2007;16:2411–2422.
- Iijima Y, Murakawa M, Kasai Y, Takahashi E, Higuchi T. Optimization transfer using surrogate objective functions. *J Comput Graph Stat*. 2012;9:1–20.
- Erdogan H, Fessler JA. Ordered subsets algorithms for transmission tomography. *Phys Med Biol*. 1999;44:2835–2851.
- Fessler JA. Statistical image reconstruction methods for transmission tomography. In: Sonka M and Fitzpatrick JM, eds. *Medical Image Processing and Analysis*. Vol. 3. Bellingham, WA: SPIE Press, 2000;1–70.
- Huber PJ. *Robust Statistics*. Berlin Heidelberg: Springer; 2011.
- Keerthi SS, Gilbert EG. Convergence of a generalized SMO algorithm for SVM classifier design. *Mach Learn*. 2002;46:351–360.
- NIST. X-Ray Mass Attenuation Coefficients. (<https://www.nist.gov/pml/x-ray-mass-attenuation-coefficients>).
- Siemens. (https://bps-healthcare.siemens.com/cv_oem/radIn.asp).
- Kak AC, Slaney M. *Principles of computerized tomographic imaging*. Philadelphia: Society for Industrial and Applied Mathematics; 2001.
- Natterer F. *The mathematics of computerized tomography*. Teubner BG. Philadelphia: Society for Industrial and Applied Mathematics. 2001.
- Niu T, Sun M, Starlack J, Gao H, Fan Q, Zhu L. Shading correction for on-board cone-beam CT in radiation therapy using planning MDCT images. *Med Phys*. 2010;37:5395–5406.
- Johns PC, Yaffe MJ. Theoretical optimization of dual-energy x-ray imaging with application to mammography. *Med Phys*. 1985;12:289–296.
- Rutherford RA, Pullan BR, Isherwood I. X-ray energies for effective atomic number determination. *Neuroradiology*. 1976;11:23–28.
- Petrongolo M, Zhu L. Noise suppression for dual-energy CT through entropy minimization. *IEEE Trans Med Imaging*. 2015;34:2646–2646.
- Richard S, Husarik DB, Yadava G, Murphy SN, Samei E. Towards task-based assessment of CT performance: system and object MTF across different reconstruction algorithms. *Med Phys*. 2012;39:4115–4122.
- Samei E, Flynn MJ, Reimann DA. A method for measuring the presampled MTF of digital radiographic systems using an edge test device. *Med Phys*. 1998;25:102–113.
- Rigie DS, La Rivière PJ. Joint reconstruction of multi-channel, spectral CT data via constrained total nuclear variation minimization. *Phys Med Biol*. 2015;60:1741–1762.
- Wunderlich A, Noo F. Image covariance and lesion detectability in direct fan-beam x-ray computed tomography. *Phys Med Biol*. 2008;53:2471–2493.
- Li Z, Yu L, Trzasko JD, et al. Adaptive nonlocal means filtering based on local noise level for CT denoising. *Med Phys*. 2014;41:011908–011908.